PHYSICAL REVIEW B VOLUME 31, NUMBER 7 1 APRIL 1985

Reentrant melting of krypton adsorbed on graphite and the helical Potts-lattice-gas model

Robert G. Caflisch* and A. Nihat Berker
Department of Physics, Massachusetts Institute of Technology, Cambridge, Massachusetts 02139

Mehran Kardar
Department of Physics, Harvard University, Cambridge, Massachusetts 02138

(Received 1 October 1984)

A model is constructed which explicitly includes the microscopic phenomena occurring in krypton adsorbed on basal graphite from submonolayer to dense-layer regimes. Second-layer adsorption is also included. The experimentally observed reentrant phase diagram, in the pressure and temperature variables, is reproduced. The problem requires different renormalization-group transformations at different length scales. Sublattice occupation and vacancy fluctuations are accounted for, starting from the length scale of the separation of adsorption sites. Dense domain-wall fluctuations, as well as their crossings and dislocations, are accounted for starting from the length scale of minimum wall separation. The physical mechanism for the reentrant phase boundary is clearly detected: At high temperatures, the first layer is disordered due to vacancies. As the system is cooled at constant pressure, condensation from the vapor permits epitaxial connectivity, and ordering takes place. Upon further cooling, further such condensation creates comparable quantities of heavy and superheavy domain walls connected by dislocations, which disrupt the long-range epitaxial ($\sqrt{3}\times\sqrt{3}$ commensurate) order. Thus, the system disorders. Upon further cooling, further condensation creates predominantly the denser superheavy walls, which start crossing. Another phase transition occurs as the superheavy walls percolate into an infinite hexagonal network. The experimentally observed maximum temperature for commensurate order is accurately obtained, with the use of the known krypton potentials. The maximum pressure is obtained for a wall energy of 83 K per unit length. In the coverage and temperature variables, our calculated phase diagram agrees quantitatively with monolayer experimental data and suggests that second-layer phase separation rather than incommensurate melting has been detected by specific-heat measurements. Effective vacancies, namely adsorbed regions of short-range disorder, are also included in the theory and extend the range of first-order transitions. The movements of atoms away from lattice-gas positions are also accounted for.

I. MOTIVATION

Krypton adsorbed on the basal surface of graphite yields a variety of phase transition phenomena, providing grounds for detailed comparison between experiments[1-13] and theory.[14-24] Here is a two-dimensional system with simple microscopic components, inert gas atoms physisorbed on a stable substrate with hexagonal modulation, which exhibits a solid commensurate with the substrate, an incommensurate solid, and a novel low-temperature fluid which is dislocation dominated.[10,21] The topology of the corresponding phase diagram and the nature of the phase boundaries, including possible multicritical phenomena,[3,16,17] have been a topic of recent interest and controversy.

This variety of phase transition phenomena is clearly due to the particular matching of the microscopic length scales of krypton and graphite. The stability of the graphite basal surface makes available the large and relatively clean systems necessary for phase transition experiments. The happy abundance of experimental information is due to a diversity of experimental probes which complement each other with respect to both the properties measured and the thermodynamic phase space covered. In fact, the recent years have witnessed a sustained evolution of knowledge and concepts as different experiments have focused on this system.

The already mentioned simplicity of the microscopic components of the krypton-on-graphite system removes the usual theorist's excuse of an untractably complicated "real" material. The microscopic potentials for an inert gas physisorbed on a stable substrate can be inferred without much room for outlandish surprises. The problem is therefore well posed and the observed interesting phenomena should all be calculated and understood with the methods of many-body physics. This paper reports some progress made in this direction.

II. BACKGROUND

A. Commensurate order and the Potts model

The graphite substrate presents a triangular array of potential minima to an adsorbing krypton atom. Each such "site" is the center of a graphite hexagon. The separation between two neighboring sites is 2.46 Å, whereas the Lennard-Jones diameter for adsorbed krypton[3] is 3.6 Å. Thus, when adsorption occurs epitaxially (namely only at the sites), nearest-neighbor pair adsorption is energetically unfavorable. The most favorable pair adsorption is at second-neighbor sites. Accordingly, the system could order into the $\sqrt{3}\times\sqrt{3}$ commensurate solid phase, by preferentially occupying one of the three sublattices of the triangular adsorption-site lattice. Various portions of Fig.

1 show the preferential occupation of sublattices *a*, *b*, or *c*.

With respect to any one sublattice, the other two sublattices are totally equivalent. This implies the permutation symmetry of a Potts model, as was first noted by Alexander,[14] who thus concluded that any critical property at the onset of $\sqrt{3}\times\sqrt{3}$ commensurate order should be discussed within context of the universality class of the two-dimensional three-state Potts model.

B. Submonolayers and the Potts-lattice-gas model

It was subsequently shown[16–18] that the connection between adsorbed layers and Potts models can be developed well beyond a universality class association, which applies only to any asymptotic critical property. This was first done in the submonolayer regime, where a given triplet of sites can be either occupied at sites *a*, *b*, or *c*, or empty. Thus, the Potts-lattice-gas model was introduced,[16,25] composed of local states $(a,b,c,0)$. By quantitatively mapping a particulate model of the layer onto the Potts-lattice-gas model, followed by a renormalization-group calculation, the phase diagram and in fact the entire statistical mechanics of the layer could be obtained to various approximations.[16,17]

C. Dense layers and the helical Potts model

The first layer of krypton can accommodate adsorption in excess of one-third of the substrate sites being occupied, by shifting from one sublattice to another via a dense wall (Fig. 1). In the neighborhood of the wall, the adatoms relax away from the substrate potential minima, so that there is no literal nearest-neighbor-site adsorption. This off-site relaxation necessitates a minimum separation between walls.[19] Nonetheless, the situation is topologically equivalent to the depiction of Fig. 1, which omits the relaxation for pedagogical purpose.

Ostlund[20] considered, along a given direction within a layer, the possibility of a wall leading from, say, sublattice *a* occupation to sublattice *b* occupation (and cyclic permutations), to the exclusion of one leading to sublattice *c* occupation. He thus called for the study of such "asymmetric" models.

In a subsequent theory,[22] the statistical importance of both types of walls, the asymmetry notwithstanding, was demonstrated. In fact, due to the interplay of excess local densities, wall crossings, and dislocations which topologically require both types of wall, this statistical importance shifts, within the phase diagram, between the two wall types. In this theory, excess local densities were explicitly related to walls, which were thereby assigned excess chemical potential as well as repulsive adatom-adatom energy. Thus, it was possible to calculate with a model which quite directly represented the microscopic picture of the dense layer. This "helical Potts model" included "heavy" and "superheavy" walls, their crossings, and their mutual annihilations at dislocation points (Fig. 1). A phase diagram was calculated, with a dense fluid phase extending to zero temperature (as had been experimentally discovered[10]) between the commensurate phase and a phase characterized by a network of superheavy walls (confirmed by experimental data analysis[12]).

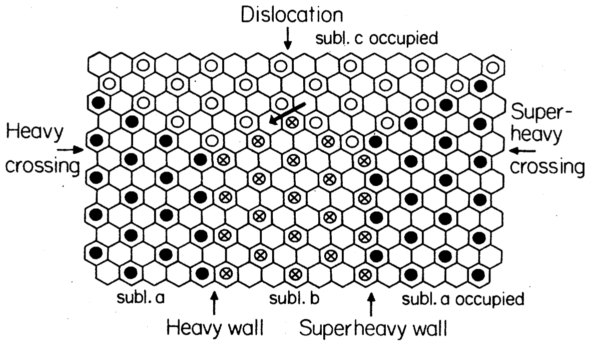

FIG. 1. Structures in a dense layer, from Ref. 22. The Burgers vector of the dislocation is shown.

III. HELICAL POTTS-LATTICE-GAS MODEL AND ITS TREATMENT

In the current work, the submonolayer and dense-layer regimes are both represented in a single model. Moreover, as interstitial atoms squeeze into the commensurate first layer to form walls, it is conceivable that second-layer adsorption becomes important, which is therefore also included in our model. Also, contact is made with the krypton vapor ambient to the adsorption system, in order to produce pressure-temperature as well as coverage-temperature phase diagrams. The successive steps of our treatment are described in this section.

A. From krypton vapor to krypton lattice gas

The chemical potential μ_V of the krypton vapor is fixed by the pressure and temperature. For the experimental conditions of interest here, it is sufficient to use the ideal-gas relation

$$\frac{\mu_V}{kT}=\ln(P\lambda^3/kT)\ , \tag{1}$$

where $\lambda=h/(2\pi mkT)^{1/2}$ is the thermal wavelength, and k and m are the Boltzmann constant and the krypton atomic mass, respectively. Under equilibrium conditions, the vapor chemical potential μ_V equals the adsorbed krypton chemical potential μ_A:

$$\mu_A=\mu_V\ . \tag{2}$$

In constructing a theory for the adsorbed phases, the many-body interactions can be coarse grained. The continuum of positions near the substrate is divided into three-dimensional cells. Consider an adatom, whose center falls within a certain cell. Insofar as determining its interactions with the other adatoms, this adatom is taken as being at the center of its cell.[26] Thus, a lattice-gas model results. The adsorbed krypton chemical potential μ_A is related to the krypton-lattice-gas chemical potential μ_L by a prefacing transformation,[27]

$$e^{\mu_L/kT}=e^{\mu_A/kT}\int_{-\infty}^{\infty}\frac{d^3p}{h^3}\int_{v_C}d^3r\,e^{-E(p,r)/kT}\ , \tag{3}$$

subsumming in the partition function the degrees of freedom of motion within the cell of volume v_C. This is calculated quantum mechanically in a harmonic approximation,

$$e^{\mu_L/kT} = e^{\mu_A/kT} \prod_{u}^{x,y,z} \sum_{n_u=0}^{\infty} e^{-\hbar\omega_u[n_u+(1/2)]/kT}$$
$$= e^{\mu_A/kT} \prod_{u}^{x,y,z} \tfrac{1}{2}\operatorname{csch}\left[\frac{\hbar\omega_u}{2kT}\right] , \qquad (4)$$

where

$$\omega_u = \sqrt{K_u/m}$$

are the characteristic frequencies in the various directions. In the present case, each graphite hexagon defines the lateral boundaries of a cell. The spring constants $K_{x,y}$ are determined for displacements from the hexagon center under a substrate-modulation potential,[28]

$$V_m(\mathbf{r}) = -\tfrac{2}{9}U_m\{\cos(\mathbf{a}_1\cdot\mathbf{r})+\cos(\mathbf{a}_2\cdot\mathbf{r}) + \cos[(\mathbf{a}_1+\mathbf{a}_2)\cdot\mathbf{r}]\} , \quad U_m = 37 \text{ K} , \qquad (5)$$

where $\mathbf{a}_{1,2}$ are the surface reciprocal-lattice vectors, and under the potential created by the occupation of the six second- neighbor sites, via the adatom-adatom potential[3]

$$V_a(r) = 4U_a\left[\left[\frac{\sigma_a}{r}\right]^{12} - \left[\frac{\sigma_a}{r}\right]^{6}\right] , \quad U_a = 145 \text{ K} , \qquad (6)$$

and

$$\sigma_a = 3.6 \text{ Å} .$$

The potentials of Eqs. (5) and (6) were also used in the previous theories.[16,17] In the vertical direction, the spring constant K_z is determined for displacements from the minimum of the substrate potential[3]

$$V_s(z) = \frac{4}{3}^{4/3} U_s\left[\left[\frac{\sigma_s}{z}\right]^{12} - \left[\frac{\sigma_s}{z}\right]^{3}\right] , \qquad (7)$$

$$U_s = 1461 \text{ K}$$

and

$$\sigma_s = 2.3 \text{ Å} .$$

The resulting frequencies are

$$\hbar\omega_x = \hbar\omega_y = 19.8 \text{ K}$$

and

$$\hbar\omega_z = 65.1 \text{ K} . \qquad (8)$$

As an aside we can calculate from these frequencies the mean-square atomic deviations away from the cell centers. In the lateral direction,

$$\langle x^2 \rangle = \frac{\hbar}{2m\omega_x}\coth\left[\frac{\hbar\omega_x}{2kT}\right] ,$$

giving (9a)

$$\langle x^2 \rangle = 0.15 \text{ Å}^2 \text{ at } T = 100 \text{ K}.$$

The small difference from 0.17 Å^2, deduced[9] from the Debye-Waller factor in the x-ray scattering experiments, is readily explained by vacancies in neighboring cells softening the lateral potential. Incidentally, these same experiments[9] reveal, at temperatures above commensurate melting, a fluid structure factor that is peaked at the commensurate position (i.e., a lattice fluid), thereby validating the lattice-gas approach. The mean-square atomic deviation in the vertical direction, for the first layer, is smaller:

$$\langle z^2 \rangle = 0.014 \text{ Å}^2 \text{ at } T = 100 \text{ K} . \qquad (9b)$$

In view of the cell lateral area of 5.24 Å^2 and the vertical microscopic scale of 2.7 Å [Eq. (7)], it appears that the atoms are quite centrally located in the cells.

An alternate, classical procedure for determining μ_L uses a "Debye volume" whose adjusted value provides a consistency check on the calculation. This will be demonstrated in our results section. As seen above, the continuum atomic motion locally affects the chemical potential μ_L and is thus included in our calculation. However, another, collective effect of continuum motion, in the presence of dense walls spanning the system, is to introduce phonons, which cause the incommensurate phase to be only algebraically ordered. Our calculation falls short of including this.

B. Second-layer adsorption

The energy gained by second-layer adsorption is estimated by a minimization. A second-layer adatom is placed in the nook provided by three first-layer adatoms in second-neighbor sites with respect to each other. Using the potentials given in Eqs. (6) and (7), an energy E_{12} is composed by adding three interlayer adatom-adatom interactions ($3\epsilon_{12}$), one second-layer adatom-substrate interaction (ϵ_{2s}), and one first-layer adatom-substrate (ϵ_{1s}) interaction. Only one of the latter is taken since there is, at saturation, approximately one first-layer adatom per second-layer adatom. This energy is minimized with respect to the vertical separations r_1 and r_2 of the two layers from the substrate. The outcome is

$$r_1 = 2.67 \text{ Å}, \quad r_2 = 5.80 \text{ Å} ,$$
$$\epsilon_{1s} = 1460 \text{ K}, \quad \epsilon_{2s} = 192 \text{ K}, \quad \epsilon_{12} = 144 \text{ K} , \qquad (10)$$
$$E_{12} = \epsilon_{1s} + \epsilon_{2s} + 3\epsilon_{12} = 2084 \text{ K} .$$

ϵ_{1s} and r_1 show almost no change from the optimal $E_1 = 1461$ K and $r = 2.68$ Å assigned by Eq. (7) to an unaccompanied first layer.

In continuing our approximate accounting of the second layer, each second-layer adatom is associated with a first-layer adatom. The adatom-adatom interactions within the second layer are treated in a mean-field approximation,

$$\rho_2=\frac{e^{(\mu_L+E_{12}+6\epsilon_{22}\rho_2 n_1)/kT}}{e^{E_1/kT}+e^{(\mu_L+E_{12}+6\epsilon_{22}\rho_2 n_1)/kT}}\ . \tag{11}$$

The conditional probability ρ_2 that a second-layer adatom will be found, given that its first-layer adatom is there, is hereby determined self-consistently. The first-layer coverage n_1 is determined directly by the renormalization-group calculation described below.[29] The total coverage is $n=n_1+n_2=n_1(1+\rho_2)$. The potential $\epsilon_{22}=134$ K is taken from Eq. (6) applied laterally to a second-neighbor-site separation.

Once more we subsum the partition function, now over the possible states of a first-layer adatom, namely with or without its second-layer companion. This prefacing transformation gives

$$e^{\mu/kT}=e^{(\mu_L+E_1)/kT}+e^{(2\mu_L+E_{12}+6\epsilon_{22}\rho_2 n_1)/kT}\ . \tag{12}$$

An effective single-layer chemical potential μ, with the effects of second-layer adsorption folded in, is hereby obtained.

We hasten to add that although we have included second-layer adsorption in an investigative spirit, our quantitative results show second-layer coverages n_2 of no more than 0.003 at the commensurate transitions and, in the temperature range of interest, no more than 0.025 at the incommensurate transitions. We shall suggest, on the other hand, that the phase separation of the second layer itself may have been detected by specific-heat measurements.

C. Renormalization-group transformations: Small length scales

We visualize the adsorption sites of the system as grouped into triplets as depicted in Fig. 2. Adatoms may occupy these triplets with chemical potential μ and mutual interactions fixed by Eq. (6). From here on, one-sixth of the occupied triplet chemical potential is assigned to each of its six nearest-neighbor bonds to the other triplets, as a book-keeping device. First, a single rescaling transformation is performed as a decimation. All triplets drawn in Fig. 2 with thin lines are summed out of the partition function. This is done in a finite-cluster approximation, shown in Fig. 3(a). For each configuration of the thick triangles, a sum is performed over the (≤ 14) configurations of the thin triangles,

$$e^{-\beta'\mathscr{H}'(s_1,t_1;s_4,t_4)}=\sum_{s_2,t_2;s_3,t_3} e^{-\beta\mathscr{H}(s_{1-4},t_{1-4})}\ , \tag{13}$$

where, for triplet i, $t_i=0$ or 1 is a lattice-gas variable which, respectively, denotes vacancy or occupancy, and in the latter case activates the Potts variable $s_i=a$, b, or c designating the occupied sublattice.[16] The nearest-neighbor exclusion and up to the fourth-neighbor interactions of the original sites are included in this decimation. One purpose of this decimation is to rotate by $\pi/6$ the lattice formed by the triplets, in order to match the domain-wall problem later on. Now, for calculational convenience, the decimated system is symmetrized,

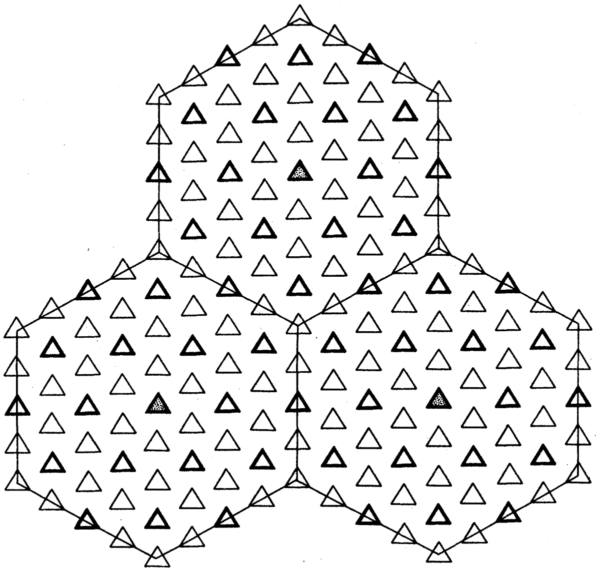

FIG. 2. Triplets (small triangles) of sites and patches (large hexagons) of sites. Dense-wall structures occur at patch length scales, so that different renormalization-group transformations are required below and above this scale. Note that nine patches (three are shown in this figure) participate into the latter transformation.

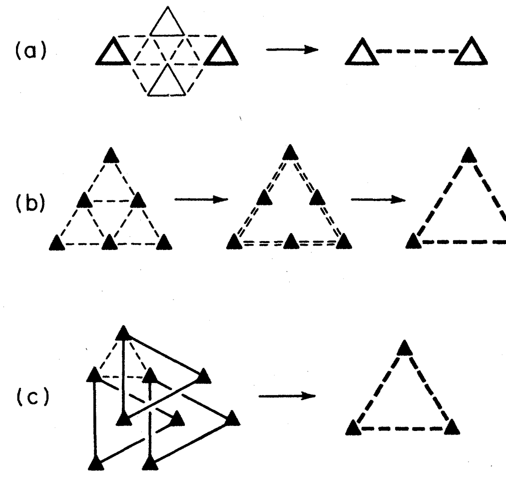

FIG. 3. Renormalization-group transformations used at different length scales. (a) Decimation performed initially to rotate the lattice by $\pi/6$. Nearest-neighbor exclusion and up to fourth-neighbor adatom interactions are included in this finite-cluster approximation. (b) Migdal-Kadanoff approximation (Ref. 16), performed twice on the Potts-lattice-gas variables to reach the dense-wall length scales. (c) Three-sublattice-cell finite-cluster approximation (Ref. 15) treating the large length scales.

$$\overline{\beta\mathcal{H}}(s_1=s_2)=\frac{\sum\limits_{s'}\beta'\mathcal{H}'(s',s')e^{-\beta'\mathcal{H}'(s',s')}}{\sum\limits_{s'}e^{-\beta'\mathcal{H}'(s',s')}}\ ,$$

$$\overline{\beta\mathcal{H}}(s_1\neq s_2)=\frac{\sum\limits_{s_1'\neq s_2'}\beta'\mathcal{H}'(s_1',s_2')e^{-\beta'\mathcal{H}'(s_1',s_2')}}{\sum\limits_{s_1'\neq s_2'}e^{-\beta'\mathcal{H}'(s_1',s_2')}}\ , \tag{14}$$

$$\overline{\beta\mathcal{H}}(s_1,0)=\tfrac{1}{3}\sum_{s'}\beta'\mathcal{H}'(s',0)\ ,$$

yielding the Potts-lattice-gas Hamiltonian,[16]

$$-\overline{\beta\mathcal{H}}(s_1,t_1;s_2,t_2)=[J\delta_{s_1s_2}+K]t_1t_2-\Delta(t_1+t_2)+G\ , \tag{15}$$

for each pair of remaining triplets, where $\delta_{s_1s_2}=1$ (0) for $s_1=s_2$ ($s_1\neq s_2$). In order to evaluate densities, it is necessary to keep track of the additive constant (G above) in the Hamiltonian.

Next follow two renormalization-group transformations, in the adaptation[16] of the Migdal-Kadanoff[30] procedure to the triangular lattice [Fig. 3(b)], which conserves the lattice directions. The corresponding recursion relations are

$$J'=\ln(R_1/R_2),\quad K'=\ln(R_2R_4/R_3^2)\ ,$$
$$\Delta'=\ln(R_4/R_3),\quad G'=4G+\ln R_4\ , \tag{16}$$

where

$$R_1=(1+x^2y^2z^2+2y^2z^2)z^2\ ,$$
$$R_2=(1+y^2z^2+2xy^2z^2)z^2\ ,$$
$$R_3=(1+xyz^2+2yz^2)z\ ,$$
$$R_4=(1+3z^2)\ ,$$

where

$$x=e^{2J},\quad y=e^{2K},\quad z=e^{-2\Delta}\ ,$$

for each transformation.

D. Heavy and superheavy walls: Helicity and trio interactions

As mentioned above, adsorption in a dense layer also occurs by the formation of dense walls (Fig. 1). To accommodate walls, adatoms must relax away from the substrate potential minima, which imposes a minimum separation between two dense walls. Villain[19] has estimated that, for krypton on graphite, this minimum separation is about five commensurate adatom separations. Thus, after the three renormalization-group transformations of the previous subsection are effected, dense walls can occur even at the smallest (renormalized) length scale. This renormalized system is composed of the triplets shaded in Fig. 2, each corresponding to patches of 144 original adsorption sites. We shall now refer to each shaded triplet, representing 144 adsorption sites, as a "patch." A triple prime will indicate the outcome of the previous three renormalization-group transformations.

A patch can be occupied (at sublattice a, b, or c) with chemical potential $-6\Delta'''$. From the previous calculation, which accounts for sublattice fluctuations made possible by vacancies, two neighboring patches can be occupied at different sublattices, with energy K'''. If they are occupied at the same sublattice, the energy is $J'''+K'''$.

Furthermore, as discussed above, dense walls can occur between the patches. The contributions to $-\beta\mathcal{H}$ of the heavy- and superheavy-wall energies are[22]

$$W_H=l(\mu/3-J_0),\quad W_s=l(2\mu/3-2J_0)\ , \tag{17}$$

where the wall length l equals 4 between patches here. The first term in Eqs. (17) is the excess chemical potential gain by the dense wall. The second term is the adatom-adatom repulsive energy price, where $J_0>0$ includes the effects of neighboring off-site relaxations. We shall here treat J_0 as a parameter to be fixed. Three heavy walls or three superheavy walls can meet at a crossing, with contribution to $-\beta\mathcal{H}$ of[22]

$$L=-3J_0/2\ . \tag{18}$$

A heavy wall and a superheavy wall can meet and annihilate at a dislocation center (Fig. 1) with no further contribution to the Hamiltonian.[22]

In sum, sublattice fluctuations are possible through vacancies in the original adsorption system and through dense walls which are permitted a relaxation region. These two phenomena are now subsumed in the partition function, for each configuration of a trio of patches:

$$\begin{aligned}
\exp[-\beta\mathcal{H}(a,a,a)]&=AZ^3X^3Y^3\ ,\\
\exp[-\beta\mathcal{H}(a,a,b)]&=AZ^3XY(Y^2+YH+YS+HS)\ ,\\
\exp[-\beta\mathcal{H}(a,b,c)]&=AZ^3(Y^3+3Y^2HC\\
&\qquad+3YH^2C^2+H^3C^3)\ ,\\
\exp[-\beta\mathcal{H}(c,b,a)]&=AZ^3(Y^3+3Y^2SC\\
&\qquad+3YS^2C^2+S^3C^3)\ ,\\
\exp[-\beta\mathcal{H}(a,a,0)]&=AZ^2XY\ ,\\
\exp[-\beta\mathcal{H}(a,b,0)]&=AZ^2(Y+H)\ ,\\
\exp[-\beta\mathcal{H}(c,b,0)]&=AZ^2(Y+S)\ ,\\
\exp[-\beta\mathcal{H}(a,0,0)]&=AZ\ ,\\
\exp[-\beta\mathcal{H}(0,0,0)]&=A\ ,
\end{aligned} \tag{19}$$

where

$$A=\exp(3G'''/2),\quad Z=\exp(-\Delta''')\ ,$$
$$X=\exp(J'''/2),\quad Y=\exp(K'''/2)\ ,$$
$$H=\exp(W_H/2),\quad S=\exp(W_S/2),\quad C=\exp(L/3)\ .$$

Exponents are divided by 2, because each patch bond participates into two patch trios. The crossing energy L is included proportionately to the number of dense walls in the configuration. Note that Eqs. (19) are a straightforward implementation of the partition function sum. A *helical Potts-lattice-gas model* with *trio interactions* is thus obtained. Helicity results from the difference between (abc)-versus-(cba) and $(ab0)$-versus-$(ba0)$ configuration energies.[22] The definition of helicity and the concomitant equations (19) are, of course, reversed in going from up-pointing trios to down-pointing trios.

E. Renormalization-group transformation: Largest length scales

The helical Potts-lattice-gas model, coupled with the trio patch interactions derived above, is solved under a renormalization-group transformation appropriate to this system. Due to the important helical configurations, the antiferromagnetic as well as ferromagnetic degrees of freedom have to be projected in the transformation. This is done in the finite-cluster approximation composed of three sublattice cells [Fig. 3(c)], introduced by Schick, Walker, and Wortis.[15]

This transformation probes the local order of each sublattice. In this process, a cell which is totally disordered conveys no ordering tendency to its neighborhood, i.e., it acts as an effective vacancy.[31] Thus, under our chosen projection operator, it is assigned the vacancy (0) cell-state.

Our projection operator $P(s',t';s_{1-3},t_{1-3})$ is defined very simply: Any cell configuration that has a majority in a, b, or c is assigned this same cell state of a, b, or c. All other cell configurations are assigned the cell state 0. The transformation is

$$e^{-6\beta'\mathscr{H}'(s'_{1-3},t'_{1-3})}=\sum_{s_{1-9},t_{1-9}} P(s'_1,t'_1;s_{1-3},t_{1-3})P(s'_2,t'_2;s_{4-6},t_{4-6})P(s'_3,t'_3;s_{7-9},t_{7-9})e^{-\beta\mathscr{H}_{\mathrm{PBC}}(s_{1-9},t_{1-9})}\,, \tag{20}$$

where the renormalized interaction is primed. Periodic boundary conditions are used on the finite cluster.[15] This is denoted, on the right-hand side of Eq. (20), by the subscript PBC of the Hamiltonian, which thereby contains 18 trio terms. Correspondingly, a factor of 6 is required in front of the Hamiltonian on the left-hand side. The renormalization-group flows are in the space of the nine energies initialized in Eqs. (19). They follow recursion relations obtained by summing Eq. (20) for the nine distinct classes of renormalized trio configurations, each sum resulting in a polynomial of up to 264 terms. Phase boundaries in the general space are found by determining the global connectivity of the flows to the fixed points.[32] Densities are evaluated by taking a derivative of the partition function with respect to the corresponding conjugate field in the unrenormalized Hamiltonian, and repeating the chain rule[16] throughout the transformations described in this section, until the densities of a phase-sink fixed point are reached. The latter densities are trivially apparent.

IV. RESULTS

A. Phase diagram in pressure and temperature

Our calculated phase diagram is drawn in Fig. 4, and has semiquantitative agreement with the experimentally determined phase transition points,[13,1–4,7,8] also shown in the figure. The maximum transition temperature of about 128 K to the commensurate phase is essentially independent of our choice of J_0 and is in very satisfactory agreement with experiment.[13] The maximum transition pressure to the commensurate phase varies with the choice of J_0. Roughly speaking, changes in J_0 affect the pressure scale as $\ln P_{\max} \sim J_0$, without affecting the shape of the phase boundaries. The experimental[13] $P_{\max}$ of 430 Torr is matched by $J_0 = 83.25$ K, an entirely reasonable value. Note from the inset that our phase boundary is in good agreement with various experiments,[1–3,7,8] over eight decades.

The low-temperature phase is characterized by a hexagonal net of superheavy walls. This is signaled by the asymptotic dominance, under repeated rescalings, of the (c,b,a) trio. This phase is identified as the incommensurate solid. Due to the approximate nature of our present treatment of the wall fluctuations, we cannot obtain here the true nature of the incommensurate melting transition. However, the fact that inside the incommensurate phase the wall net is superheavy rather than heavy is important physical information. This was first predicted by our original treatment[22] using the helical Potts model and confirmed by experimental data analysis[12] and by subsequent numerical simulation study.[24]

The fluid phase is found between the commensurate and incommensurate solids,[33] as was originally discovered in the synchrotron x-ray scattering experiments of Moncton *et al.*[10] In fact, our fluid phase shows reentrant

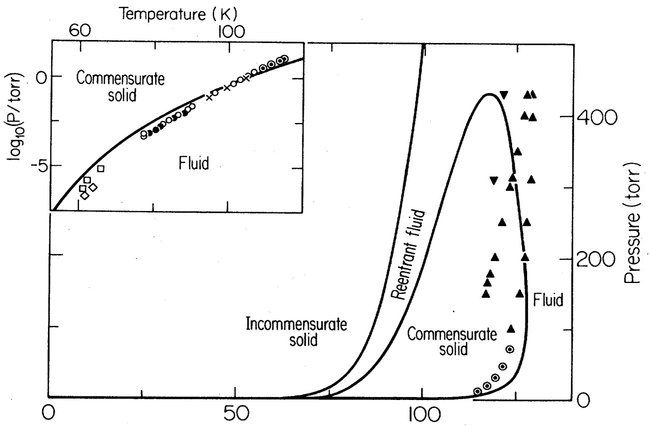

FIG. 4. Calculated reentrant phase diagram (curves) in the pressure and temperature variables. Also shown are experimentally determined phase transition points: commensurate (▲) and incommensurate (▼) melting from x-ray scattering (Ref. 13), volumetric [Ref. 1 (○), Ref. 2 (●), Ref. 3 (×), Ref. 4 (⊙)], low-energy electron diffraction [Ref. 7 (□)], and transmission-high-energy electron diffraction [Ref. 8 (◇)].

behavior as a function of temperature, in agreement with the similar experiments of Specht *et al.*[13] The microscopic mechanisms underlying these phenomena will be discussed in the next subsection. The order of the phase transitions will be discussed in Sec. IV C.

We briefly return here to the contribution, to the chemical potential, due to motion within each lattice-gas cell. This was calculated quantum mechanically in Eq. (4). An alternate classical expression for this prefacing transformation is

$$e^{\mu_L/kT} = e^{\mu_A/kT} \int_{-\infty}^{\infty} \frac{d^3p}{h^3} \int_{v_C} d^3r\, e^{-[p^2/2m + U_C(\mathbf{r})]/kT} , \quad (21)$$

where $U_C(\mathbf{r}) \geq 0$ is an effective single-body potential which controls the intracell motion of the atom. The above can be approximated by

$$\begin{aligned} e^{\mu_L/kT} &\simeq e^{\mu_A/kT} \int_{-\infty}^{\infty} \frac{d^3p}{h^3} \int_{v_D} d^3r\, e^{-p^2/2mkT} \\ &= e^{\mu_A/kT} v_D \lambda^{-3} , \end{aligned} \quad (22)$$

where $v_D \leq v_C$ is a "Debye" volume, reflecting mean-square deviations from the cell center. Combining with Eqs. (1)–(3),

$$\frac{\mu_L}{kT} = \ln(P v_D / kT) . \quad (23)$$

Pressure only appears multiplied with the Debye volume v_D. This route is further investigated, after fixing J_0 at 83.25 K. The experimental $P_{\max}$ then determines $v_D \simeq 0.34$ Å^3. Thus, the desirable qualitative agreement is seen with the volume of the mean-square displacements, $\pi\langle x^2\rangle 2(\langle z^2\rangle)^{1/2} = 0.14$ Å^3, calculated with Eq. (9a) at the temperature 117 K of $P_{\max}$.

B. Wall, dislocation densities, and the reentrance mechanism

The calculated densities, along the phase boundaries, of heavy and superheavy walls are shown in Fig. 5. A density of 1 corresponds to maximal wall accommodation, meaning that all patches of the system in Sec. III D are completely surrounded with the given type of wall.

Around the commensurate phase boundary, heavy- and superheavy-wall densities are roughly equal, crossing each other twice. Both densities show a slight increase with melting. Both densities become substantial only well into the high-pressure side of the maximum temperature.

On the other hand, along the incommensurate boundary, the superheavy-wall density is considerably larger than the heavy-wall density, consistently with the superheavy-net nature of the incommensurate phase. Similarly, the superheavy-wall density shows a slight decrease with this melting, whereas the heavy-wall density again shows a slight increase.

The calculated dislocation (i.e., meeting and annihilation of a heavy wall and a superheavy wall) densities along the phase boundaries are shown in Fig. 6. There is a slight increase in the dislocation density at all melting points. As the phase boundary is followed starting from the low-temperature low-pressure limit, the dislocation density becomes noticeable only beyond the maximum commensurate melting temperature. The dislocation den-

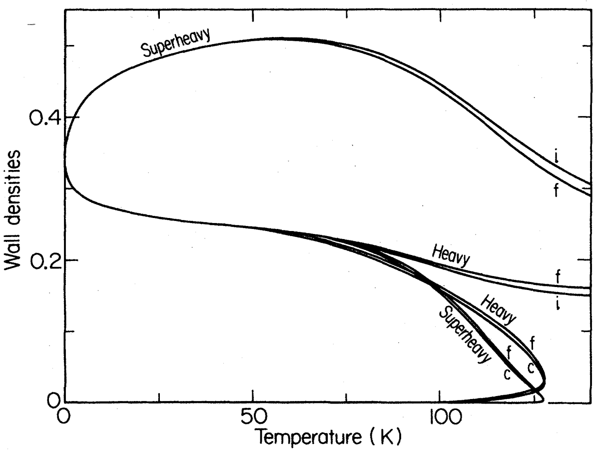

FIG. 5. Calculated heavy- and superheavy-wall densities on the phase boundaries, given as fractions of maximum accommodation in the first layer. Curves corresponding to the onsets of the commensurate, incommensurate, and fluid phases are indicated with the letters, *c*, *i*, and *f*. Heavy and superheavy walls are equally abundant on (the dense side of) the commensurate boundary, whereas superheavy walls dominate the incommensurate phase.

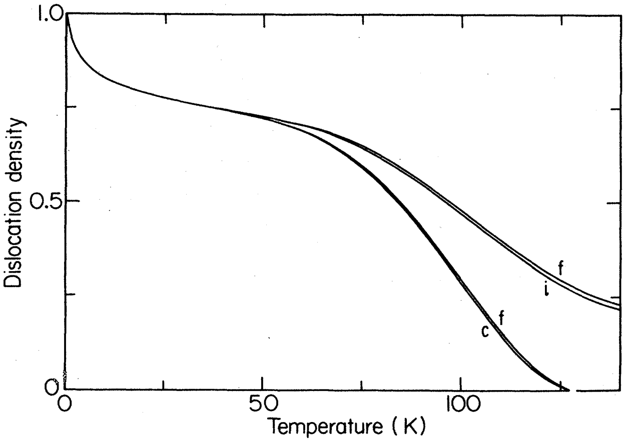

FIG. 6. Calculated density of dislocations, where a heavy wall and a superheavy wall annihilate, on the phase boundaries. Curves corresponding to the onsets of the commensurate, incommensurate, and fluid phases are indicated with the letters *c*, *i*, and *f*. These densities are given as fractions of maximum accommodation in the first layer, which is realized in the zero-temperature dense fluid (also see Fig. 7). Our model is equivalent, at that point, to the antiferromagnetic three-state Potts model on the Kagomé lattice and at zero temperature. This system has an infinite ground-state degeneracy, which explains the lack of order even at zero-temperature. The dislocation density is negligible on the dilute side of the maximum transition temperature.

sity increases to its maximum value of 1 as the boundary to the dense fluid reaches zero temperature. This corresponds to the system in Sec. III D with every patch trio surrounding a dislocation. Equivalently, the system is disordered with the many equivalent configurations in which walls meander with alternate heavy and superheavy segments, at essentially the minimal separation between each other, and with the proviso that they do not cross (Fig. 7). The model reduces here to the antiferromagnetic three-state Potts model on the Kagomé lattice and at zero temperature. The Potts states are the no-wall, heavy-wall, or superheavy-wall states of each patch boundary. The dislocation density decreases from 1 as the incommensurate boundary is followed to high temperature.

The mechanism for the reentrance is apparent from this information. Consider a constant pressure scan. At high temperatures, due to vacancies, the layer cannot achieve connectivity and thus is disordered. As temperature is lowered, adatoms condense from the vapor, connectivity is achieved, and ordering takes place. As temperature is further lowered, further condensation from the vapor creates walls, which disrupt long-range commensurate order.[34] The system disorders. At this reentrant commensurate melting, the fluid is dense and is dominated by dislocations. It contains a tangle of walls which are equally composed of heavy and superheavy segments and which are mostly self-avoiding (few crossing, see Fig. 8). As the temperature is further lowered, still keeping the pressure constant, further condensation from the vapor creates predominantly the denser superheavy walls, which now start crossing. When the superheavy walls percolate into an infinite network, the incommensurate solid phase replaces the fluid phase.

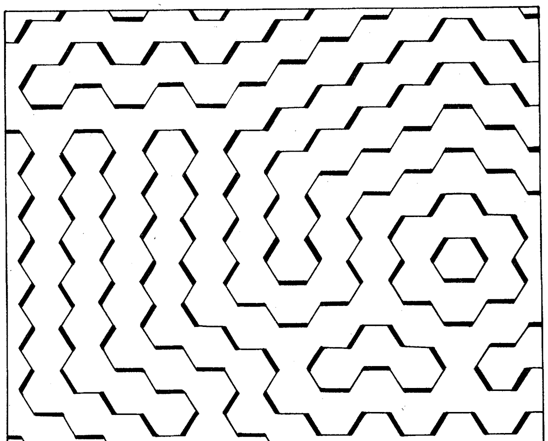

FIG. 7. One of the many degenerate fully-dislocated configurations which occur in the zero-temperature dense fluid. Heavy- and superheavy-wall segments are drawn with thin and thick lines, respectively. Walls meander with such segments alternating between dislocations, are maximally packed, but never cross. The model is equivalent here to the antiferromagnetic three-state Potts model on the Kagomé lattice.

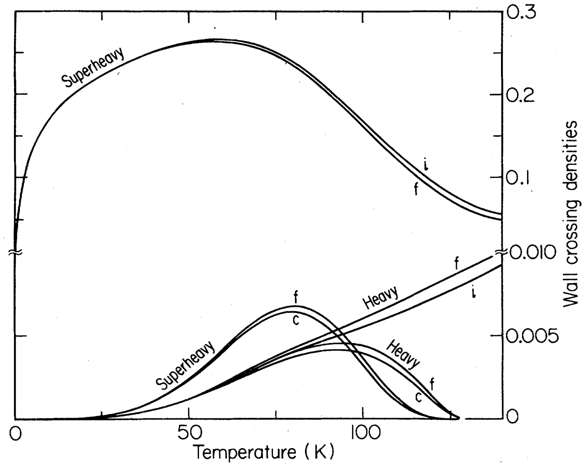

FIG. 8. Calculated heavy- and superheavy-wall-crossing densities on the phase boundaries, given as fractions of maximum accommodation in the first layer. Curves corresponding to the onsets of the commensurate, incommensurate, and fluid phases are indicated with the letters *c*, *i*, and *f*. Thus, walls do not cross in the zero-temperature dense fluid. Note the scale change: only superheavy crossings at incommensurate melting are appreciable.

C. Phase diagram in coverage and temperature

The phase diagram in the total (first- and second-layer) coverage and temperature variables is shown in Figs. 9 and 10. The coverage of $n=1$ is equivalent to one complete $\sqrt{3}\times\sqrt{3}$ commensurate layer, i.e., one-third of the

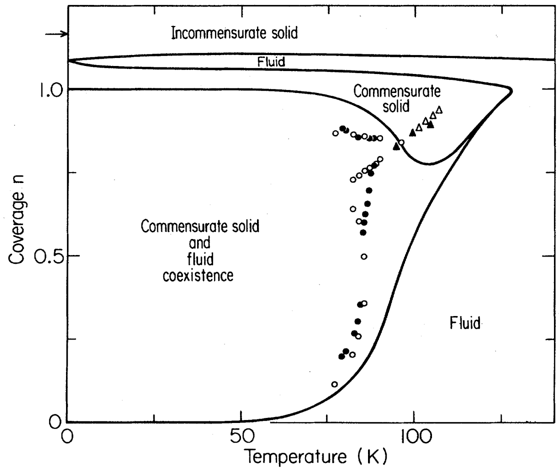

FIG. 9. Calculated phase diagram (curves) in the total coverage and temperature variables. The coverage $n=1$ is equivalent to a complete $\sqrt{3}\times\sqrt{3}$ commensurate layer (one-third of the sites occupied). The arrow indicates the coverage $n=1.167$ of a maximally dense layer, which is saturated with superheavy walls. Experimentally determined phase transition points, from volumetric measurements, are also shown. Reference 1 (△) and Ref. 3 (▲) report, above 95 K, imperceptible coexistence ranges at the transitions which are nonetheless clearly defined by isotherm slope discontinuities. At lower temperatures, Ref. 1 (○) and Ref. 2 (●) show coexistence ranges. See also Fig. 10.

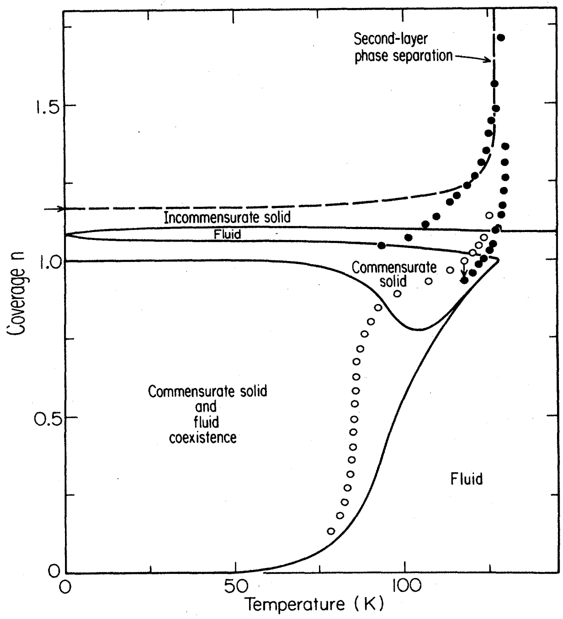

FIG. 10. Calculated phase diagram (curves) in the total coverage and temperature variables. The coverage $n=1$ is equivalent to a complete $\sqrt{3}\times\sqrt{3}$ commensurate layer (one-third of the sites occupied). The arrow indicates the coverage $n=1.167$ of a maximally dense layer, which is saturated with superheavy walls. The dilute fluid continuously evolves to the dense, dislocation-dominated fluid which reaches zero temperature between the commensurate and incommensurate phases. A theoretical curve for phase separation in the second layer is drawn with dashes. Experimentally determined points of specific-heat singularity are also shown. Reference 5 (○) gives points without desorption correction, which when accounted, causes shift to the desorption-corrected Ref. 6 (●) points, as shown with the arrow at 118 K. See discussion in Sec. IV C.

sites occupied. The arrow shows the coverage, within our model, of a totally dense first layer, which is saturated with superheavy walls and which has $n=1.167$.

We first discussed the submonolayer region. Volumetric (isotherm) experimental data[1-3] is shown in Fig. 9. Note that the original experiments of Thomy and Duval[1] showed liquid-gas coexistence (the middle dip in the open circles). In fact, Larher[2] insisted in subsequent work to place such a region between two of his narrowly separated isotherms, in the total absence of experimental evidence. Based on an objective evaluation of his isotherms, on specific-heat measurements[5] (see Fig. 10), and on theoretical calculations,[16,17] it is now believed that no such structure, but a single fluid phase, exists.

Our calculated submonolayer coexistence boundary is in quite good agreement with the experimental data. This is quite satisfactory, also in view of the further fact that renormalizing the lattice-gas adatom-adatom interaction (not done here) to account for intracell motion decreases[17] the transition temperatures by about 10%.

All of the calculated phase boundaries in Figs. 4 and 9 are first order, as could have been apparent from our previous discussion of wall, dislocation, and crossing densities. However, the submonolayer coexistence region pinches off at 105 K, collapsing to effectively zero width in the high-temperature, high-coverage, and incommensuration regions. We believe that our large-length-scale renormalization-group transformation (Sec. III E) is biased for first-order transitions. (This transformation gives a first-order transition even for the pure nearest-neighbor three-state Potts model, but with a jump in $\langle \delta_{s_1 s_2} \rangle$ of only 0.08.) Thus, there could in reality be a multicritical point somewhere along the collapsed coexistence region, followed by a true single boundary line of second order, as was seen in previous renormalization-group theories[16,17,22] (which did not include effective vacancies and were therefore biased for second-order transitions). We are currently pursuing the development of improved transformations. We note that a coexistence gap of 5% in coverage at a temperature as high as 115 K was reported more recently.[4] This disagreement with other experiments is probably due to experimental defects such as temperature inhomogeneities across the sample, an effect which was previously predicted.[17,18]

X-ray scattering experiments[13] have reported correlation lengths of 17 and 111 Å (compare with the commensurate adatom separation of 4.26 Å) in the fluid at temperatures above and below the commensurate phase. We have estimated the ratio of the correlation lengths at $T=120.5$ K, $P=14.3$ Torr and $T=104.5$ K, $P=279$ Torr, above and below our commensurate phase, by counting the number of renormalization-group transformations needed to reach a defined neighborhood of the fluid-sink fixed point. We found that two more transformations are needed for the lower-temperature point, giving a correlation-length ratio of $(\sqrt{3})^2=3$, quite short of the experiment. We note, incidentally, that if true critical behavior were to occur at the commensurate melting of krypton on graphite, rather precise experiments would be expected for a critical exponent determination, since the critical region of the three-state Potts model is estimated[35] to be an order of magnitude smaller than that of the Ising model, in two dimensions.

Comparison with the specific-heat experimental data of Butler *et al.*[5,6] is made in Fig. 10. The open circles are transition points reported[5] without the "desorption" correction, which is made for the black circles.[6] Under this correction, the open circles are shifted as shown with the arrow at 118 K. Thus, agreement with our calculation is quite good along the entire boundary stretching from zero to one monolayer. Note the absence of liquid-gas coexistence. The other branch of submonolayer coexistence is not detected by specific heat measurements (whereas it can be inferred from the volumetric measurements[1,2]). A similar situation exists with nitrogen on graphite.[36] We consider this an unresolved situation which requires direct specific-heat calculations from our part. These are currently being pursued.

The higher-coverage region raises other interesting questions. In our calculation, the dense fluid phase (which extends from the dilute fluid phase) reaches zero temperature between the commensurate and incommensurate phases.[33] The incommensurate melting is essentially driven by coverage. At this point, we have to disagree with some of the original interpretation[6] of the specific-heat experiments. It had been suggested that the singularities driven by temperature around 1.5 layers are due to incommensurate melting. This is unlikely for two reasons: First, incommensurate melting should exhibit an essential singularity invisible to specific-heat scans.[37] Second, a first layer saturated with walls has to maintain the hexagonal wall structure and thus cannot melt. Thermal promotion of adatoms from first to second layer can only occur at the much higher temperatures of about $E_1-27J_0/56-\epsilon_{2s}-3\epsilon_{12}=797$ K [see Eqs. (10)]. Thus, for the temperatures of concern here, the incommensurate boundary has to be coverage driven and essentially parallel to the temperature direction, at a coverage less than $n=1.17$, as is our calculated boundary. One caveat to these conclusions, in terms of a would-be adatom reservoir not in the vapor, will be given below.

A much more likely cause of one set of high-coverage specific-heat singularities is dense and dilute second-layer phase separation, which is certain to occur. The dashed line in Fig. 10 shows the phase-separation curve obtained for a lattice-gas model, by mapping onto the exact solution of the triangular Ising model.[38] [This phase separation also follows from Eq. (11) in our calculational procedure.] The nearest-neighbor lattice-gas energy was adjusted to 140 K, to yield the critical temperature of 127 K. This energy is reasonable, as it is expected to be around the first-layer energy of 145 K [Eq. (6)]. The flat top of the second-layer phase separation curve is a reflection of the Ising critical exponent $\beta=\frac{1}{8}$. On the other hand, the dense phase of the second layer has a choice of two sublattices.[39] Thus, if tricritical fluctuations of the $(q=2)$-state Potts-lattice-gas (i.e., spin-1 Ising or Blume-Emery-Griffiths[40,32]) type were present, the exponent $\beta_u=\frac{1}{4}$ would be applicable.[31,41] This exponent value would give a more rounded phase separation curve near its maximum temperature, which is perhaps seen in the exhibited points of specific-heat singularity.

All of the specific-heat data is not satisfactorily understood, however. For example, the low-temperature, high-coverage fluid phase seen in the x-ray scattering experiments[10] and reproduced in our calculation cannot be fit anywhere in this data. On the other hand, the reentrant commensurate boundary in coverage space, suggested by these authors,[6] is possible under the following physical circumstance: In our theory, the reentrant commensurate boundary in pressure space is obtained because the krypton vapor acts as an adatom reservoir. If, additionally, there exists an adatom reservoir which is adsorbed but not part of the layers undergoing phase transitions, with a reservoir adsorption energy of about $E_1-27J_0/56-100$ K $=1321$ K, the reentrance and incommensuration boundaries attributed to the specific-heat data would be plausible. Candidates for such an adsorbed reservoir are capillary condensation and/or adsorption onto a large number of irregular and small substrate facets. A renormal- ization-group study,[42] which considered a distribution of finite facets and matched specific-heat data for helium on krypton-plated graphite,[39] points in the latter direction. We stress, on the other hand, that the second layer cannot be this reservoir, because its energy of $\epsilon_{2s}+3\epsilon_{12}=624$ K is not favorable enough. Indeed, we calculate no more than 3% second-layer coverage anywhere on the first-layer melting boundaries of Fig. 10. The second-layer phase separation mentioned above is fueled not by atoms departing from the first layer, but by those condensing from the vapor.

ACKNOWLEDGMENTS

We have benefited from discussions with R. J. Birgeneau, E. D. Specht, and M. Sutton. This research was supported, at the Massachusetts Institute of Technology, by Army Research Office Contract No. DAAG29-81-K0029 and by National Science Foundation (NSF) Grant No. DMR-83-02419 and, at Harvard, by NSF Grant No. DMR-82-07431. We also acknowledge the support of the Fannie and John Hertz Foundation for R. G. C., the Alfred P. Sloan Foundation for A. N. B., and the Harvard Society of Fellows for M. K.

---

*Present address: Schlumberger-Doll Research Center, Old Quarry Road, Ridgefield, Connecticut 06877.

[1] A. Thomy and X. Duval, J. Chim. Phys. **66**, 1966 (1969); **67**, 286 (1970); **67**, 1101 (1970).

[2] Y. Larher, J. Chem. Soc. Faraday Trans. 1 **70**, 320 (1974).

[3] F. A. Putnam and T. Fort, Jr., J. Phys. Chem. **79**, 459 (1975); **81**, 2164 (1977); F. A. Putnam, T. Fort, Jr., and R. B. Griffiths, *ibid.* **81**, 2171 (1977).

[4] Y. Larher and A. Terlain, J. Chem. Phys. **72**, 1052 (1980).

[5] D. M. Butler, J. A. Litzinger, G. A. Stewart, and R. B. Griffiths, Phys. Rev. Lett. **42**, 1289 (1979).

[6] D. M. Butler, J. A. Litzinger, and G. A. Stewart, Phys. Rev. Lett. **44**, 466 (1980).

[7] S. C. Fain, Jr. and M. D. Chinn, J. Phys. (Paris) **38**, C4-99 (1977); M. D. Chinn and S. C. Fain, Jr., Phys. Rev. Lett. **39**, 146 (1977).

[8] P. S. Schabes-Retchkiman and J. A. Venables, Surf. Sci. **105**, 536 (1981).

[9] R. J. Birgeneau, E. M. Hammons, P. Heiney, P. W. Stephens, and P. M. Horn, in *Ordering in Two Dimensions,* edited by S. K. Sinha (Elsevier, New York, 1980), p. 29.

[10] D. E. Moncton, P. W. Stephens, R. J. Birgeneau, P. M. Horn, and G. S. Brown, Phys. Rev. Lett. **46**, 1533 (1981).

[11] M. Nielsen, J. Als-Nielsen, J. Bohr, and J. P. McTague, Phys. Rev. Lett. **47**, 582 (1981).

[12] P. W. Stephens, P. A. Heiney, R. J. Birgeneau, P. M. Horn, D. E. Moncton, and G. S. Brown, Phys. Rev. B **29**, 3512 (1984).

[13] E. D. Specht, M. Sutton, R. J. Birgeneau, D. E. Moncton, and P. M. Horn, Phys. Rev. B **30**, 1589 (1984).

[14] S. Alexander, Phys. Lett. **A54**, 353 (1975).

[15] M. Schick, J. S. Walker, and M. Wortis, Phys. Rev. B **16**, 2205 (1977).

[16] A. N. Berker, S. Ostlund, and F. A. Putnam, Phys. Rev. B **17**, 3650 (1978).

[17] S. Ostlund and A. N. Berker, Phys. Rev. Lett. **42**, 843 (1979).

[18] A. N. Berker, in *Ordering in Two Dimensions,* edited by S. K. Sinha (Elsevier, New York, 1980), p. 9.

[19] J. Villain, in *Ordering in Strongly Fluctuating Condensed*

Matter Systems, edited by T. Riste (Plenum, New York, 1980), p. 221.

[20] S. Ostlund, Phys. Rev. B **24**, 398 (1981).

[21] S. N. Coppersmith, D. S. Fisher, B. I. Halperin, P. A. Lee, and W. F. Brinkman, Phys. Rev. Lett. **46**, 549 (1981).

[22] M. Kardar and A. N. Berker, Phys. Rev. Lett. **48**, 1552 (1982).

[23] R. J. Gooding, B. Joos, and B. Bergersen, Phys. Rev. B **27**, 7669 (1983).

[24] F. F. Abraham, W. E. Rudge, D. J. Auerbach, and S. W. Koch, Phys. Rev. Lett. **52**, 445 (1984).

[25] The Potts-lattice-gas model was in fact subsequently necessary to elucidate the changeover of the order of the phase transitions in q-state Potts models, and led to the determination of exact tricritical exponents. See Ref. 31.

[26] M. E. Fisher, Rep. Prog. Phys. **30**, 615 (1967).

[27] A. N. Berker, Phys. Rev. B **12**, 2752 (1975).

[28] G. L. Price and J. A. Venables, Surf. Sci. **59**, 509 (1976).

[29] At first-order phase boundaries, the average n_1 of the two coexisting phases was used. In the region where second-layer adsorption could be important, the values of n_1 in the two coexisting phases differed by less than 2 parts in 10^3.

[30] A. A. Migdal, Zh. Eksp. Teor. Fiz. **69**, 1457 (1975) [Sov. Phys.—JETP **42**, 743 (1976)]; L. P. Kadanoff, Ann. Phys. (N.Y.) **100**, 359 (1976).

[31] B. Nienhuis, A. N. Berker, E. K. Riedel, and M. Schick, Phys. Rev. Lett. **43**, 737 (1979); A. N. Berker and D. Andelman, J. Appl. Phys. **53**, 7923 (1982).

[32] A. N. Berker and M. Wortis, Phys. Rev. B **14**, 4946 (1976).

[33] In Ref. 22, it was shown that coadsorption of a smaller atomic species such as deuterium causes, by lowering crossing energies, a direct first-order transition between the commensurate and incommensurate solids at low temperatures, as in the experiments of Ref. 11.

[34] An alternate reentrance mechanism was independently suggested by J. G. Dash and R. J. Muirhead (unpublished). In contrast to our mechanism, this mechanism invokes a diluted first layer on both sides of the commensurate phase. A first-to-second layer promotion is required as temperature is lowered, with which we cannot agree, since this promotion involves a net energy expenditure of about 800 K (see Sec. IV D). We are grateful to Professor Dash for a stimulating discussion of our opposing microscopic pictures.

[35] This is estimated as follows. Let the Ising critical point be at a separation K from its fixed point in general interaction space. Straightforward renormalization-group analysis then shows that the critical region around the Ising critical point is given by $\tau_I=\delta(K/\delta)^{y_1/y_2}$, where δ delimits the linear scaling region around the fixed point, and $y_1>0$ and $y_2<0$ are the relevant and leading irrelevant eigenvalue exponents. A similar expression holds for the three-state Potts model in two dimensions. Using for our estimate the same values of K and δ, taking a ratio, and substituting the values of the eigenvalue exponents from Ref. 41, we find $\tau_P/\tau_I=(\delta/K)^{4/3}$. In other words, the $(q=3)$-state Potts model is closer to the marginality (see Ref. 31) of $q_c=4$, compared with the Ising model $(q=2)$. Therefore, more rescalings are necessary to reach the fixed point. Furthermore, since the Potts temperature direction is more relevant than the Ising one, deviations from criticality get amplified more in each rescaling.

[36] A. D. Migone, M. W. H. Chan, K. J. Kiskanen, and R. B. Griffiths, J. Phys. C **16**, L1115 (1983).

[37] See Fig. 5 of A. N. Berker and D. R. Nelson, Phys. Rev. B **19**, 2488 (1979) for the invisible essential singularity in the specific heat of the related XY model.

[38] R. J. Baxter, *Exactly Solved Models in Statistical Mechanics* (Academic, London, 1982).

[39] M. J. Tejwani, O. Ferreira, O. E. Vilches, Phys. Rev. Lett. **44**, 152 (1980); W. Kinzel, M. Schick, and A. N. Berker, in *Ordering in Two Dimensions,* edited by S. K. Sinha (Elsevier, New York, 1980), p. 381.

[40] M. Blume, V. J. Emery, and R. B. Griffiths, Phys. Rev. A **4**, 1071 (1971).

[41] B. Nienhuis, J. Phys. A **15**, 199 (1982).

[42] D. J. E. Callaway and M. Schick, Phys. Rev. B **23**, 3494 (1981).